ACS APPLIED NANO MATERIALS

www.acsanm.org Article

WS_2 2D Semiconductor Down to Monolayers by Pulsed-Laser Deposition for Large-Scale Integration in Electronics and Spintronics Circuits

Florian Godel, Victor Zatko, Cécile Carrétéro, Anke Sander, Marta Galbiati, Aymeric Vecchiola, Pierre Brus, Odile Bezencenet, Bernard Servet, Marie-Blandine Martin, Bruno Dlubak,* and Pierre Seneor*

Cite This: *ACS Appl. Nano Mater.* 2020, 3, 7908−7916 Read Online

ACCESS | Metrics & More | Article Recommendations

ABSTRACT: We report on the achievement of a large-scale tungsten disulfide (WS_2) 2D semiconducting platform derived by pulsed-laser deposition (PLD) on both insulating substrates ($SrTiO_3$), as required for in-plane semiconductor circuit definition, and ferromagnetic spin sources (Ni), as required for spintronics applications. We show thickness and phase control, with highly homogeneous wafer-scale monolayers observed under certain conditions, as demonstrated by X-ray photoelectron spectroscopy and Raman spectroscopy mappings. Interestingly, growth appears to be dependent on the substrate selection, with a dramatically increased growth rate on Ni substrates. We show that this 2D-semiconductor integration protocol preserves the interface integrity. Illustratively, the WS_2/Ni electrode is shown to be resistant to oxidation (even after extended exposure to ambient conditions) and to present tunneling characteristics once integrated into a complete vertical device. Overall, these experiments show that the presented PLD approach used here for WS_2 growth is versatile and has a strong potential to accelerate the integration and evaluation of large-scale 2D-semiconductor platforms in electronics and spintronics circuits.

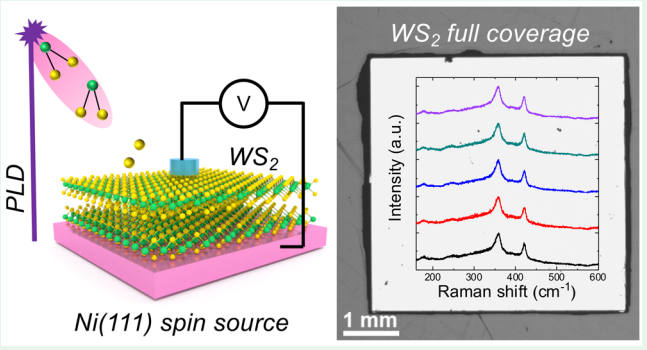

KEYWORDS: *2D semiconductors, WS_2, pulsed-laser deposition, spintronics, X-ray photoemission spectroscopy, Raman spectroscopy*

INTRODUCTION

2D materials are attractive not only for their atomically precise thickness definition but also for their numerous properties with potential applications in electronics,[1−3] optoelectronics,[4−6] and spintronics.[7,8] Overcoming the issue of graphene's lack of a band gap, large families of 2D semiconductors have been highlighted for epitaxy-free technologies and size-weight-power-and-cost reduction. Their strong potential for discrete components currently developed with the usual semiconductors (including III−Vs or ultrathin dielectrics) arouses interest in the microtechnology field.[9−12] For radio-frequency and optoelectronics applications, transition-metal dichalcogenide (TMDC) 2D semiconductors, such as molybdenum disulfide (MoS_2) and tungsten disulfide (WS_2), offer wide tunability of their electronic properties and provide a large variety of band gaps.[13] Concerning spintronics, a strong potential of 2D materials is anticipated for magnetic tunnel junction (MTJs) spin-valve devices, as currently exploited in magnetoresistive random-access memories (MRAMs)[14] and recently highlighted for spin logics as well as low-power neuromorphic and stochastic calculations.[15−19] Indeed, the spin properties are expected to be tuned by the insertion of atomically thin 2D materials in MTJs. For instance, the proximity of 2D layers, such as graphene, hexagonal boron nitride (h-BN) or WS_2, with ferromagnetic spin sources has already been demonstrated to allow enhanced spin-filtering properties.[20−22] Further tailoring of the perpendicular magnetic anisotropy, spin−orbit torque (SOT), and topological spin textures such as skyrmions is also expected.[23−25]

However, in order to accelerate 2D semiconductors families exploration and their technological integration, reliable and reproducible wafer-scale synthesis processes have to be identified and developed beyond exfoliation.[26,27] This has

Received: May 23, 2020
Accepted: July 29, 2020
Published: July 29, 2020

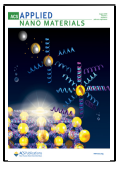

https://dx.doi.org/10.1021/acsanm.0c01408
ACS Appl. Nano Mater. 2020, 3, 7908−7916

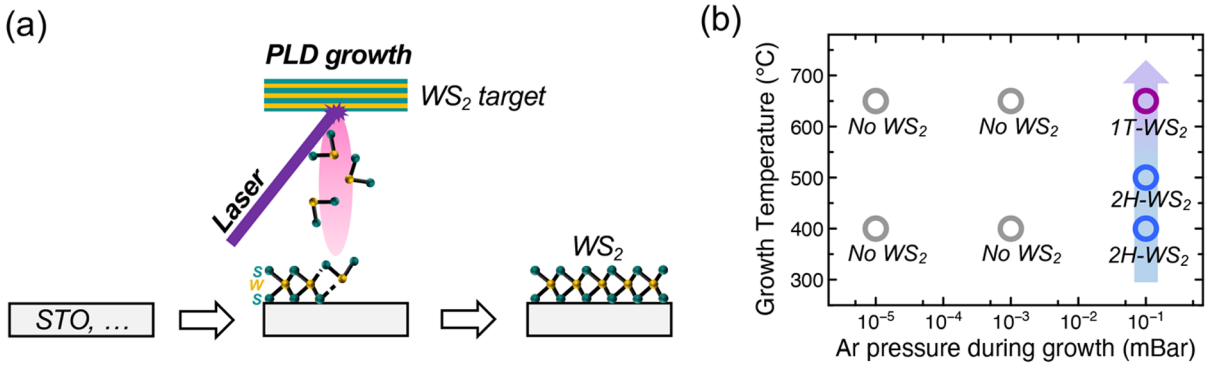

Figure 1. (a) Schematic view of the PLD process for WS_2 growth. We work under 10^{-5}–10^{-1} mbar of Ar pressure. The WS_2 target is preablated and the substrate preheated to reach the growth temperature (400–650 °C). Growth is carried using a 355 nm Nd:YAG laser at 2.5 Hz pulse frequency and a nominal power of 80 mJ/pulse. After growth, the resulting sample is cooled in Ar before being unloaded from the PLD chamber. (b) Explored growth conditions (Ar pressure and substrate temperature), pinpointing the key role of high Ar pressure for the growth of crystalline WS_2.

been previously illustrated, for instance, in the case of graphene and 2D insulator h-BN, where going from exfoliated flakes to wafer-scale monolayers[28−30] allowed large-scale device integration. Following these early successes, most current efforts for the growth of 2D semiconductors are focused on chemical vapor deposition (CVD) processes,[31,32] while pioneer studies have highlighted the strong potential of alternative approaches like molecular beam epitaxy (MBE)[33−35] and pulsed-laser deposition (PLD).[36−38]

In this study, we present the fabrication and integration of large-scale WS_2 layers, demonstrating the pertinence of PLD growth for the investigation of 2D semiconductor platforms. PLD is a convenient method to grow wafer-scale stoichiometric materials,[39−43] and we have identified protocols leading to WS_2 growth (Figures 1 and 2). We achieve wafer-scale homogeneous layers on different substrates, down to the monolayer, as demonstrated by Raman spectroscopy (Figure 3). We underline the benefit of this large-scale approach for spintronics applications, showing preservation of the Ni interface (Figure 4) and first integration of the PLD-grown WS_2 layer in a vertical device heterostructure, where it behaves as a tunnel barrier (Figure 5). With PLD being a particularly versatile technique, it is expected that this study will open the way to the growth of many 2D compounds among TMDC families, with access to virtually any simple or alloyed TMDC as well as layered heterostructures, and to the exploration of their integration in functional devices.

RESULTS AND DISCUSSION

In Figure 1a, a sketch of the PLD process is depicted. We use a homemade PLD setup based on a Nd:YAG laser with a tripled frequency (355 nm) and a UHV chamber with a base pressure of 1×10^{-8} mbar.[39−43] We attempt growth with a high-purity Ar gas pressure in the 10^{-5}–10^{-1} mbar range during processing. We make use of a commercial stoichiometric target of WS_2 (Neyco) shot with 80 mJ laser power pulses (2.5 Hz repetition frequency) for 1 min. The target is preablated before deposition in an Ar atmosphere. The distance between the target and substrate is fixed to a large value of 70 mm to mitigate the kinetics and growth rate, looking for good crystallization conditions.[44,45] Several growth temperatures are explored in the 400–650 °C range. After growth, the sample is cooled for 1 h in an Ar atmosphere.

The first set of WS_2 layers are grown on common insulating crystalline substrates, such as $SrTiO_3$ (STO) and sapphire, using the PLD process described above. To investigate the structural properties of the resulting WS_2 layer, we perform Raman spectroscopy experiments with a 514 nm laser. Indeed, WS_2 presents a typical Raman signature (see below), and this first analysis by Raman spectroscopy allows us to already figure out which growth conditions are required for the crystallization of WS_2 layers.[46] As detailed in Figure 1b, we do not observe typical Raman signatures of WS_2 for the lower 10^{-5} and 10^{-3} mbar Ar pressures and for both 400 and 650 °C growth temperatures. In these laser ablation conditions, the vapor plume at the surface of the substrate is probably too dense and too energetic to allow ordered WS_2 growth.[44,45] At a higher Ar pressure of 10^{-1} mbar, with increased confinement of the vapor plume and slowed growth kinetics, the crystallization leads to well-defined WS_2 films, as checked by X-ray photoelectron spectroscopy (XPS) and Raman spectroscopy (see below). Following Loh et al.,[36] to identify the chemical nature of the WS_2 layers, we perform specific XPS measurements (Figure 2). These are carried out using a Mg source and based on spectra with a 30 eV pass energy. We focus on the energy core levels of S 2p (from 158 to 167 eV) and W 4f (from 28 to 41 eV). Contributions of the S^{2-} states of S atoms in WS_2 can be observed at 162 eV (S $2p_{3/2}$) and 163.2 eV (S $2p_{1/2}$) with a typical energy splitting of 1.2 eV. For 400–550 °C growths, we also observe W^{4+} states, for which contributions are located at 32.4 eV ($4f_{7/2}$) and 34.6 eV ($4f_{5/2}$): these energies are the signature of crystalline 2H-WS_2 in a hexagonal semiconductor phase.[36] We note that no oxidation of the WS_2 film is observed, with an extracted W/S ratio of 0.5. This is further confirmed by the Raman analyses (see below). For 650 °C growth, the doublet peak is shifted at 31 and 33.2 eV, corresponding to the appearance of the 1T phase. We base our interpretation of the XPS spectra on reference studies[36,47] to attribute the evolution of the phase toward 1T. These first experiments confirm the possibility of deriving WS_2 by tuning the PLD process to slower kinetics (a large target–substrate distance and a high background Ar pressure), with a crystallographic phase controlled by the substrate temperature. In the following, we will focus on the 2H-WS_2 semiconducting phase.

In Figure 3, we focus on the thickness of the resulting layer and the homogeneity of coverage. We demonstrate the

https://dx.doi.org/10.1021/acsanm.0c01408
ACS Appl. Nano Mater. 2020, 3, 7908−7916

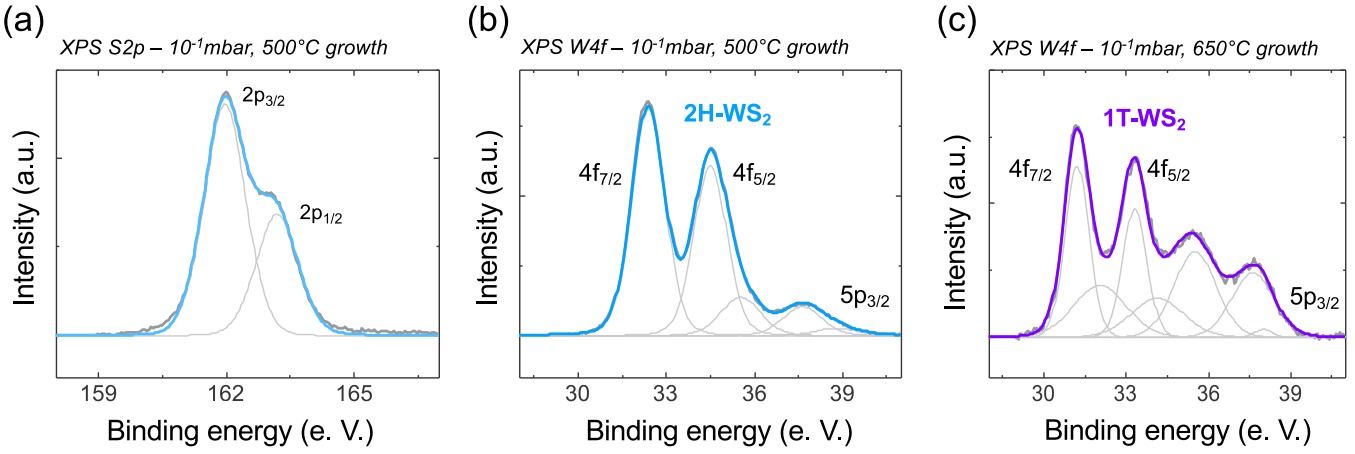

Figure 2. XPS analysis of the PLD-grown WS_2 layers carried out using a Mg source and based on five spectra with 20 eV pass energy. Spectra acquired for (a) S 2p (500 °C), (b) W 4f (500 °C), and (c) W 4f (650 °C) components confirm crystallization of the WS_2 layer at 10^{-1} mbar of Ar pressure. XPS spectra are calibrated on the C 1s peak energy (284.5 eV). Following Loh et al.,[36] these spectra show 2H-WS_2 phase crystallization during 500 °C growth and shift toward 1T-WS_2-rich crystallization at 650 °C growth. The core level of S 2p (from 158 to 167 eV) in part a shows the S 2p peak with distinguished level S $2p_{3/2}$ located at 162 eV and S $2p_{1/2}$ at 163.2 eV with a typical energy splitting of 1.2 eV, which are directly connected to the S^{2-} states of S atoms in WS_2. Parts b and c show the W 4f core level (from 28 to 41 eV) and present the W 4f bond environment: W^{4+} states, whose contributions are located at 32.4 eV ($4f_{7/2}$) and 34.6 eV ($4f_{5/2}$) with a typical energy splitting of 2.2 eV, are the signature of crystalline 2H-WS_2 in the hexagonal semiconductor phase. In part c, the peak located at 31 eV with a corresponding doublet peak at 33.2 eV reveals the presence of metallic W atoms in the W^{0+} states, which correspond to the 1T metallic phase. From the integrated and corrected intensities of both S 2p and W 4f (W^{4+} and W^{0+}) energy states, a stoichiometry of 0.5 is confirmed and corresponds to the 1W/2S expected for WS_2, confirming its good quality. Higher energy peaks at 35.6 eV, and its doublets are attributed to the W^{6+} state and 38.4 eV to W $5p_{3/2}$.

homogeneity of our 1 cm^2 samples by a large-scale Raman mapping study: no variation is observed over the whole sample surface. Raman spectroscopy has been shown to be a versatile method to determine the number of grown TMDC layers (see, for instance, refs 22 and 46), deduced from the peak intensity ratio. The Raman signature of WS_2 has been well documented in the literature in a large variety of situations, and we base our analyses on key references such as refs 46 and 48. We note that we have previously characterized WS_2 on spin sources and clearly correlated the Raman signature, obtained with the same setup as that used in this study, with atomic force microscopy (AFM) data,[22] allowing us to extract precise information about the grown layers. The number of WS_2 layers is deduced from the ratio $2LA/A_{1g}$ of the intensity of the 2LA mode (longitudinal acoustic mode enhanced with a 514 nm laser) relative to the A_{1g} mode (first-order phonon mode, corresponding to A_1' for an odd number of layers). Indeed, WS_2 is expected to be a monolayer for $2LA/A_{1g} > 1.3$ when probed with a 514 nm laser.[22] Similarly, it is possible to spot multilayer patches because bilayers have $2LA/A_{1g} \approx 1$ and thicker layers have $2LA/A_{1g} < 1$ (down to 0.5). Figure 3c shows Raman spectra recorded on our WS_2/STO(001) sample. Interestingly, the observed $2LA/A_{1g}$ ratio is above 1.3 and is the signature of monolayer WS_2. We carry out similar measurements on different locations of the 1 cm^2 sample without noticing any difference: the whole surface appears covered with monolayer WS_2. To ensure the continuous coverage of WS_2, we map the Raman signal of a large region with a step of 1 μm between each point. We extract the $2LA/A_{1g}$ ratio at each position and derive a $2LA/A_{1g}$ ratio map. Figure 3e shows the $2LA/A_{1g}$ map, which shows continuous coverage of WS_2 on STO. The first observation is that no holes are visible in the deposited WS_2 layer (no red patch on the mapping of Figure 3e). This already underlines the quality of the film derived by PLD and the pertinence of our approach. Furthermore, the WS_2 film is shown to be mostly monolayer (dark-gray area with a $2LA/A_{1g}$ ratio of >1.3 in Figure 3e) with rare patches of multilayers (light-gray spots in Figure 3e). Overall, we observe continuous WS_2 coverage, with monolayers representing >99.6% of the surface on our insulating 1 cm^2 STO substrate. AFM shows low roughness and 0.8 nm thickness, in line with the expected WS_2 layered structure from Raman analyses, as observed in other studies.[22] This initial PLD growth result is to be compared with state-of-the-art CVD and MBE studies, where closing TMDC 2D films on large scales and limiting the growth to one layer have been reported to be particularly challenging.[31,32,44,45]

Next, we investigate the WS_2 growth on a ferromagnetic electrode, as required for integration in spintronics devices.[22,49−51] We prepare Ni(111) crystalline layers on a sapphire (0001) substrate using a sputtering technique. The sapphire substrate is annealed at 700 °C in a vacuum inside the sputtering chamber for 30 min before proceeding to the 80 nm Ni film deposition at 2.5×10^{-3} mbar of Ar pressure with a typical deposition rate of 2 Å/s. The crystallinity of the Ni film is confirmed by X-ray diffraction: Ni crystallizes fully along the ⟨111⟩ orientation.[52] The sample is then transferred to the PLD/XPS chamber. The transfer is done in air, and Ni surface is expected to be oxidized, as confirmed by XPS. The Ni(111)/sapphire substrate is first annealed under 0.1 mbar of Ar pressure at 500 °C for 20 min. This annealing step allows one to reduce the Ni substrate and clean it from any atmospheric pollution, and it has been found to be key to reaching our results. Then, we proceed to WS_2 growth under the same conditions as those previously used for the STO substrate (sample-to-target distance = 70 mm, laser power = 80 mJ/pulse, laser frequency = 2.5 Hz, and deposition time = 1 min). Figure 3d shows Raman spectra recorded on WS_2/Ni(111)/sapphire: it shows the clear signature of multilayer WS_2 with a typical $2LA/A_{1g}$ ratio in the 0.5−1.3 range. This is observed consistently on any part of the 1 cm^2 sample. To confirm the

https://dx.doi.org/10.1021/acsanm.0c01408
ACS Appl. Nano Mater. 2020, 3, 7908−7916

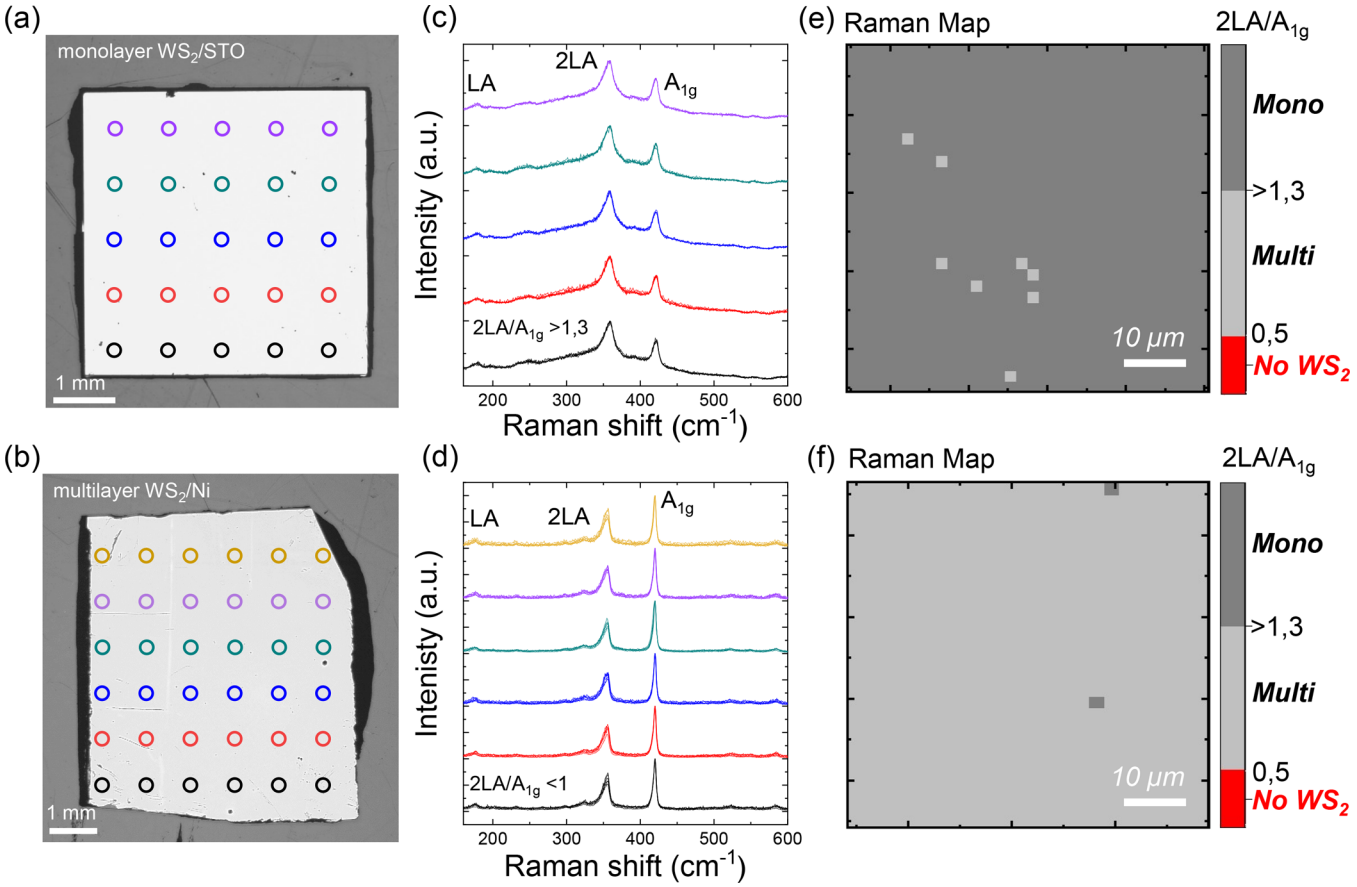

Figure 3. Raman analyses of the resulting WS_2 growth. Raman surveys are presented by sets of colored circles spaced by 1 mm steps drawn on optical images of (a) WS_2/STO(001) and (b) WS_2/Ni(111) samples. Circles represent the locations where Raman spectra of WS_2 have been recorded with a 514 nm laser. These Raman surveys for both WS_2/STO and WS_2/Ni samples are presented in parts c and d, respectively. The Raman spectra have been drawn on top of each other for each line of measurements (represented by one given color). The Raman spectra show characteristic phonon peaks of longitudinal modes (LA at 176 cm^{-1} and 2LA at 352 cm^{-1}) and a first-order mode (A_{1g} at 417 cm^{-1}). The typical signature of a WS_2 monolayer is obtained with a $2LA/A_{1g}$ ratio of >1.3 in part c and a multilayer with $2LA/A_{1g}$ ratio <0.5 in part d. (e) $2LA/A_{1g}$ ratio Raman map of the same WS_2/STO(001) sample with Raman spectra recorded over an area of 60 × 60 μm^2 with a 1 μm step. Each 2LA and A_{1g} Raman peak is fitted using a mixed Gaussian−Lorentzian curve in order to extract the intensity. The Raman map shows 99.6% coverage of the STO by a WS_2 monolayer with a few spots of multilayer WS_2. (f) $2LA/A_{1g}$ Raman map of the same WS_2/Ni(111) sample recorded under the same conditions as those in part e. The full coverage of WS_2 on both the STO and Ni layers is thus confirmed with both large-scale (c and d) and local (e and f) Raman maps.

homogeneity and covering of WS_2 onto Ni(111), we perform a Raman mapping of the $2LA/A_{1g}$ ratio (Figure 3f) with the same parameters as those used for the WS_2/STO sample in Figure 3e. As for STO, it appears that the WS_2 layer fully covers the surface of Ni. WS_2 is mainly multilayer (>3 layers) with rare occurrence of monolayer (less than 0.1%). The reactivity and catalytic behavior of the metallic surface of Ni seems to enhance the growth rate of WS_2 compared to the oxide surface of STO, where monolayer growth is observed for the same conditions. As such, we are able to observe stable multilayer and monolayer growth. Overall, we show here that the PLD approach is able to offer control over the phase and thickness of the grown 2D semiconductor, depending on the growth parameters and selected substrates, with a full coverage over the 1 cm^2 sample of the 2D monolayer material.

To illustrate the potential of wafer-scale 2D semiconductor PLD growth, we focus now on the WS_2 sample grown on a Ni ferromagnetic spin source. We investigate the impact of WS_2 on the Ni spin source layer surface using XPS measurements. These measurements are carried out using a Mg source (1253 eV) and recorded with a 30 eV pass energy. Figure 4 shows the Ni core-level XPS spectra of Ni(111) without (Figure 4a) and with (Figure 4b) WS_2 growth on top, after being exposed for 7 days to ambient conditions. For bare Ni films, significant peaks of the nickel oxide signature are observed between 853 and 867 eV for the Ni $2p_{3/2}$ level (between 871 and 885 eV for Ni $2p_{1/2}$, respectively).[53,54] Remarkably, identical XPS measurements performed on the WS_2-covered Ni sample show no sign of Ni oxidation, and a clear metallic signature is revealed with metallic peaks of Ni $2p_{3/2}$ at 852.6 eV and Ni $2p_{1/2}$ at 869.9 eV. Our data show no evolution of the Ni(111) state after WS_2 growth, excluding, in particular, reactivity with S and O. This highlights that the WS_2 layer is thus able to preserve the Ni metallic state underneath and protect it from oxidation under ambient air conditions, a challenging issue with other approaches such as exfoliation or CVD transfer. This initial observation demonstrates that our PLD approach has a strong potential for the fabrication of 2D-based hybrid heterostructures (such as spin sources) for spintronics. This direct-growth approach by PLD unlocks the exploration of the interface's crafting by proximity effects, leading to the definition of novel 2D-based "spinterfaces" as discussed by

https://dx.doi.org/10.1021/acsanm.0c01408
ACS Appl. Nano Mater. 2020, 3, 7908−7916

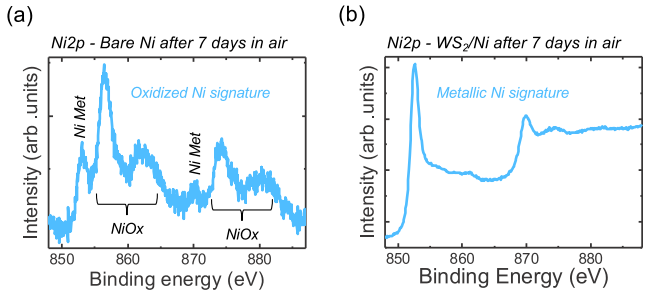

Figure 4. XPS spectra of the Ni 2p core level recorded with a Mg source (1253 eV) for (a) a bare Ni(111) layer and (b) WS_2-covered Ni(111) after extended exposure to oxidative conditions (7 days in air). Bare Ni(111) self-oxides under room conditions. Once passivated with WS_2 layers, it remains metallic. XPS spectra are calibrated on the C 1s peak energy (284.5 eV). This result shows the high quality and continuity of our WS_2 layer, which is able to act as an oxidation barrier preserving the full metallicity of underlying Ni.

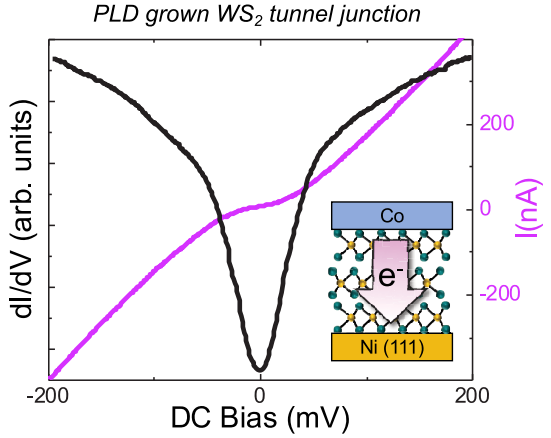

Figure 5. Ni/WS_2/Co heterostructure fabricated by taking a contact on top of the WS_2/Ni films. Device $I(V)$ and dI/dV characterizations lead to the observation of typical nonlinear tunneling behavior. This confirms the high quality of the WS_2 and WS_2/Ni interfaces, further highlighting the potential of PLD-grown WS_2 as a tunnel barrier in spin-valve devices.

Galbiati et al.[55] for organic compounds and observed for the 2D insulator h-BN,[21] taking advantage of rich families of 2D TMDCs to open perspectives for control of the extracted spin-polarized currents.

Finally, we demonstrate the pertinence of our PLD growth scheme by fabricating a complete device heterostructure and validating the WS_2 ultrathin layer as a tunnel barrier. As schematically shown in the inset of Figure 5, we define a top Co contact over the WS_2/Ni layers. The junctions are defined by laser photolithography with a size of about 1 μm^2, and the top Co/Au electrode is evaporated over the whole sample. Ag paste is used to manually mask each contact, and a reactive ion etching step is carried out to isolate the junctions and allow bonding (see the process details in refs 22 and 51). This device allows one to probe the vertical tunneling transport characteristics through the PLD-grown WS_2 layer. In Figure 5, we present the typical current $I(V)$ and its first derivative dI/dV transport measurements recorded at 4 K in such a device. Both $I(V)$ and dI/dV present shapes that are typical characteristics of tunnel junctions. Observation of the tunneling current in these devices, integrating the transport properties over a whole contact area which would be compromised by any defect included in the junction, highlights the high quality of the grown material. This tunneling behavior has been observed reproducibly in several junctions, underlining the quality and homogeneity of the grown WS_2 material, as expected from the Raman mapping study. The PLD-grown WS_2 layer is thus shown to be compatible with vertical device integration. It is striking to observe that tunneling characteristics are obtained with this WS_2 material in light of the usual difficult engineering development required to reach tunneling conditions with oxides.[56−58] This result further highlights 2D materials as strong candidates toward a tunneling device configuration. We thus demonstrate the use of our WS_2 thin film grown by the PLD approach as a tunnel barrier: the remarkable high homogeneity (absence of a pinhole) in the WS_2 thin layer grants a well-defined tunneling behavior in devices, proving the pertinence of our PLD-based protocol to fabricate vertical junctions based on 2D semiconductors. Hence, our study is an important first step toward the exploration of 2D semiconductors families integration in charge and spin devices. Many properties of these 2D materials in electronics and spintronics devices remain to be studied: doping, thickness, material composition including alloying and stacked heterostructures, crystallite size, phase, morphology, etc. PLD is a relevant technique for flexible direct integration and the junction's fabrication. By highlighting the particular PLD integration approach, which effectively unlocks the integration of TMDC with delicate spintronics materials, we believe exploration of the performance of these 2D semiconductors for spintronics will be eased, with perspectives, for instance, for the induced proximity effect on spin transport channels,[59,60] control of skyrmionic spin textures,[61,62] expected exploitation of strong spin−orbit coupling for SOT-MRAM technologies, etc.[63−65] We believe it will now lead a large community to explore these different aspects.

CONCLUSION

In conclusion, we identify here conditions for the successful growth of wafer-scale WS_2 films by PLD, with high homogeneity and down to the monolayer limit. The 2D semiconductor growth is demonstrated on both insulating (STO) and metallic (Ni) substrates. Remarkably, WS_2 films grown directly on spin-polarized Ni electrodes are shown to protect the underneath Ni from oxidation, fulfilling a key requirement for spintronics applications and highlighting the wafer-scale WS_2 homogeneity. This is even further highlighted by the use of this PLD-grown WS_2/Ni interface as a tunnel layer in a vertical device structure.

We rely on Raman spectroscopy and XPS characterizations to extract material information on relevant scales, successfully leading *in-fine* to the fabrication of functional tunnel junctions. The PLD technique has been used by several groups in the past to grow 2D materials[38,66−72] including WS_2, as reported by Tian et al.[73] following initial reports.[36,37,47] In our work, we show that this growth can be controlled down to monolayers on large surfaces and, importantly, directly integrated on delicate metallic spin sources, while preserving their metallic nature with no interfacial oxidation, a necessary step toward their exploitation for spintronics. Our main target is to highlight PLD growth as a testbed for 2D semiconductors, demonstrating that large-scale growth (in contrast with mechanical exfoliation) can be achieved directly on the target substrate (in contrast with the usual transfer of CVD-grown materials). They are thus compatible with direct device

https://dx.doi.org/10.1021/acsanm.0c01408
ACS Appl. Nano Mater. 2020, 3, 7908−7916

integration. This has been previously shown to be the key to unleashing spin-transport performances of 2D materials in MTJs.[20,21] It should enable further acceleration of the screening of the particular properties of 2D semiconductors. This PLD approach will be a key enabler for tailoring of the composition (either in the form of alloys or layered heterostructures) and achieving thickness control through growth conditions such as the number of laser pulses or pressure (see, for instance, refs 38 and 68), a performance that remains otherwise difficult to reach. By integrating the resulting WS_2/Ni electrode in a functional vertical device and using the WS_2 layer as a tunnel barrier, we demonstrate the high quality of the PLD-grown material and its compatibility with device integration. A key result of our study is that PLD is indeed able to provide a high-quality 2D platform for device testing. Furthermore, the easy change of material targets should also strongly accelerate the development of novel 2D heterostructures. This should broaden even one step further, associating 2D materials with spintronics oxide materials such as, for instance, YIG[43] and LSMO.[41] Overall, our study opens the perspective of evaluating the performance of wafer-scale grown 2D semiconductors among large TMDC families (including alloyed TMDCs and heterostructures) in electronics and spintronics devices.

At a time where current SOT-MRAM technologies,[14,74] as well as proposed post-CMOS spin logics[16] and magnonics[43] schemes, are looking for large spin−orbit materials like TMDCs[75,76] for the control of spin transport, PLD growth thus holds an impressively strong perspective. PLD offers the outstanding potential to control 2D TMDC film parameters (number of layers, phase, etc.) and integrate them directly with oxides as well as metals. It, hence, provides an unprecedented edge for the exploration of hybrid metal/oxide heterostructures embedding 2D semiconductors. We thus believe that the development of these schemes will benefit from co-integration in complex heterostructures of functional oxides already grown by PLD (ferromagnetic insulators, half-metals, ferroelectric and multiferroic materials, etc.) and TMDC material families, as allowed by the presented PLD approach.

METHODS

WS_2 2D-Semiconductor Growth. We use a homemade PLD setup based on a UHV chamber with a base pressure of 1.10^{-8} mbar and a Nd:YAG laser with the typical wavelength reduced to 355 nm. The distance between the target and substrate is 70 mm. We shoot a commercial stoichiometric target of WS_2 (Neyco) at 0.1 mbar of Ar pressure with 80 mJ laser power and 7 ns pulse length and a laser pulse frequency of 2.5 Hz. Before deposition, the substrate is preheated in the PLD chamber under 0.1 mbar of Ar pressure to clean and prepare the surface. In particular, for the Ni layer, the preheating step is performed at 500 °C for 20 min to remove O from Ni and obtain a metallic surface for WS_2 growth. The target is also preablated before growth for 5 min at 0.1 mbar of Ar pressure to recover the clean WS_2 target surface. Deposition is then performed by ablating the target for 1 min, while keeping a sample-to-target distance of 70 mm (laser power = 80 mJ and laser frequency = 2.5 Hz). The sample is cooled in the PLD chamber for 1 h under 0.1 mbar of Ar pressure before further manipulation.

WS_2-Based Device Fabrication. The bottom Ni(111) electrode is sputtered at 700 °C on sapphire (customized Plassys setup). The large-scale WS_2 layer is grown directly on top of it by PLD. Microjunctions are defined by laser lithography using a UVIII resist. Finally, the top Au-capped Co (15 nm) electrode is deposited by e-beam evaporation.

AUTHOR INFORMATION

Corresponding Authors

Bruno Dlubak − *Unité Mixte de Physique, CNRS, Thales, Université Paris-Saclay, 91767 Palaiseau, France*; orcid.org/0000-0001-5696-8991; Email: bruno.dlubak@cnrs-thales.fr

Pierre Seneor − *Unité Mixte de Physique, CNRS, Thales, Université Paris-Saclay, 91767 Palaiseau, France*; Email: pierre.seneor@cnrs-thales.fr

Authors

Florian Godel − *Unité Mixte de Physique, CNRS, Thales, Université Paris-Saclay, 91767 Palaiseau, France*; orcid.org/0000-0003-1741-2741

Victor Zatko − *Unité Mixte de Physique, CNRS, Thales, Université Paris-Saclay, 91767 Palaiseau, France*; orcid.org/0000-0002-2475-8866

Cécile Carrétéro − *Unité Mixte de Physique, CNRS, Thales, Université Paris-Saclay, 91767 Palaiseau, France*

Anke Sander − *Unité Mixte de Physique, CNRS, Thales, Université Paris-Saclay, 91767 Palaiseau, France*

Marta Galbiati − *Unité Mixte de Physique, CNRS, Thales, Université Paris-Saclay, 91767 Palaiseau, France*

Aymeric Vecchiola − *Unité Mixte de Physique, CNRS, Thales, Université Paris-Saclay, 91767 Palaiseau, France*

Pierre Brus − *Unité Mixte de Physique, CNRS, Thales, Université Paris-Saclay, 91767 Palaiseau, France; Thales Research and Technology, 91767 Palaiseau, France*

Odile Bezencenet − *Thales Research and Technology, 91767 Palaiseau, France*

Bernard Servet − *Thales Research and Technology, 91767 Palaiseau, France*

Marie-Blandine Martin − *Unité Mixte de Physique, CNRS, Thales, Université Paris-Saclay, 91767 Palaiseau, France*

Complete contact information is available at: https://pubs.acs.org/10.1021/acsanm.0c01408

Notes

The authors declare no competing financial interest.

ACKNOWLEDGMENTS

This project has received funding from the European Union's H2020 Excellent Science under grant agreements No 785219 and 881603. This research is supported by a public grant overseen by the French National Research Agency (ANR) as part of the "Investissements d'Avenir" program (Labex NanoSaclay; ANR-10-LABX- 0035).

REFERENCES

(1) Lemme, M. C.; Li, L. J.; Palacios, T.; Schwierz, F. Two-Dimensional Materials for Electronic Applications. *MRS Bull.* **2014**, *39* (8), 711−718.

(2) Fiori, G.; Bonaccorso, F.; Iannaccone, G.; Palacios, T.; Neumaier, D.; Seabaugh, A.; Banerjee, S. K.; Colombo, L. Electronics Based on Two-Dimensional Materials. *Nat. Nanotechnol.* **2014**, *9* (10), 768−779.

(3) Chhowalla, M.; Jena, D.; Zhang, H. Two-Dimensional Semiconductors for Transistors. *Nat. Rev. Mater.* **2016**, *1* (11), 16052.

(4) Cheng, J.; Wang, C.; Zou, X.; Liao, L. Recent Advances in Optoelectronic Devices Based on 2D Materials and Their Heterostructures. *Adv. Opt. Mater.* **2019**, *7* (1), 1800441.

(5) Kang, S.; Lee, D.; Kim, J.; Capasso, A.; Kang, H. S.; Park, J.-W.; Lee, C.-H.; Lee, G.-H. 2D Semiconducting Materials for Electronic and Optoelectronic Applications: Potential and Challenge. *2D Mater.* **2020**, *7* (2), 022003.

(6) Montanaro, A.; Mzali, S.; Mazellier, J.-P.; Bezencenet, O.; Larat, C.; Molin, S.; Morvan, L.; Legagneux, P.; Dolfi, D.; Dlubak, B.; Seneor, P.; Martin, M.-B.; Hofmann, S.; Robertson, J.; Centeno, A.; Zurutuza, A. Thirty Gigahertz Optoelectronic Mixing in Chemical Vapor Deposited Graphene. *Nano Lett.* **2016**, *16* (5), 2988−2993.
(7) Seneor, P.; Dlubak, B.; Martin, M.-B.; Anane, A.; Jaffres, H.; Fert, A. Spintronics with Graphene. *MRS Bull.* **2012**, *37* (12), 1245−1254.
(8) Piquemal-Banci, M.; Galceran, R.; Martin, M.-B.; Godel, F.; Anane, A.; Petroff, F.; Dlubak, B.; Seneor, P. 2D-MTJs: Introducing 2D Materials in Magnetic Tunnel Junctions. *J. Phys. D: Appl. Phys.* **2017**, *50* (20), 203002.
(9) Castellanos-Gomez, A. Why All the Fuss about 2D Semiconductors? *Nat. Photonics* **2016**, *10* (4), 202−204.
(10) Manzeli, S.; Ovchinnikov, D.; Pasquier, D.; Yazyev, O. V.; Kis, A. 2D Transition Metal Dichalcogenides. *Nat. Rev. Mater.* **2017**, *2* (8), 17033.
(11) Schram, T.; Smets, Q.; Groven, B.; Heyne, M. H.; Kunnen, E.; Thiam, A.; Devriendt, K.; Delabie, A.; Lin, D.; Lux, M.; Chiappe, D.; Asselberghs, I.; Brus, S.; Huyghebaert, C.; Sayan, S.; Juncker, A.; Caymax, M.; Radu, I. P. WS_2 Transistors on 300 Mm Wafers with BEOL Compatibility. *European Solid-State Device Research Conference*; Editions Frontieres, 2017; pp 212−215; DOI: 10.1109/ESSDERC.2017.8066629.
(12) Radu, I. Atom-Thick Transistors. *IEEE Spectrum* **2020**, *57* (2), 44−49.
(13) Ataca, C.; Şahin, H.; Ciraci, S. Stable, Single-Layer MX_2 Transition-Metal Oxides and Dichalcogenides in a Honeycomb-like Structure. *J. Phys. Chem. C* **2012**, *116* (16), 8983−8999.
(14) Khvalkovskiy, A. V.; Apalkov, D.; Watts, S.; Chepulskii, R.; Beach, R. S.; Ong, A.; Tang, X.; Driskill-Smith, A.; Butler, W. H.; Visscher, P. B.; Lottis, D.; Chen, E.; Nikitin, V.; Krounbi, M. Basic Principles of STT-MRAM Cell Operation in Memory Arrays. *J. Phys. D: Appl. Phys.* **2013**, *46* (7), 074001.
(15) Behin-Aein, B.; Datta, D.; Salahuddin, S.; Datta, S. Proposal for an All-Spin Logic Device with Built-in Memory. *Nat. Nanotechnol.* **2010**, *5* (4), 266−270.
(16) Manipatruni, S.; Nikonov, D. E.; Lin, C. C.; Gosavi, T. A.; Liu, H.; Prasad, B.; Huang, Y. L.; Bonturim, E.; Ramesh, R.; Young, I. A. Scalable Energy-Efficient Magnetoelectric Spin-Orbit Logic. *Nature* **2019**, *565* (7737), 35−42.
(17) Torrejon, J.; Riou, M.; Araujo, F. A.; Tsunegi, S.; Khalsa, G.; Querlioz, D.; Bortolotti, P.; Cros, V.; Yakushiji, K.; Fukushima, A.; Kubota, H.; Yuasa, S.; Stiles, M. D.; Grollier, J. Neuromorphic Computing with Nanoscale Spintronic Oscillators. *Nature* **2017**, *547* (7664), 428−431.
(18) Mizrahi, A.; Hirtzlin, T.; Fukushima, A.; Kubota, H.; Yuasa, S.; Grollier, J.; Querlioz, D. Neural-like Computing with Populations of Superparamagnetic Basis Functions. *Nat. Commun.* **2018**, *9* (1), 1533.
(19) Borders, W. A.; Pervaiz, A. Z.; Fukami, S.; Camsari, K. Y.; Ohno, H.; Datta, S. Integer Factorization Using Stochastic Magnetic Tunnel Junctions. *Nature* **2019**, *573* (7774), 390−393.
(20) Martin, M.-B.; Dlubak, B.; Weatherup, R. S.; Yang, H.; Deranlot, C.; Bouzehouane, K.; Petroff, F.; Anane, A.; Hofmann, S.; Robertson, J.; Fert, A.; Seneor, P. Sub-Nanometer Atomic Layer Deposition for Spintronics in Magnetic Tunnel Junctions Based on Graphene Spin-Filtering Membranes. *ACS Nano* **2014**, *8* (8), 7890.
(21) Piquemal-Banci, M.; Galceran, R.; Godel, F.; Caneva, S.; Martin, M.-B.; Weatherup, R. S.; Kidambi, P. R.; Bouzehouane, K.; Xavier, S.; Anane, A.; Petroff, F.; Fert, A.; Dubois, S. M.-M.; Charlier, J.-C.; Robertson, J.; Hofmann, S.; Dlubak, B.; Seneor, P. Insulator-to-Metallic Spin-Filtering in 2D-Magnetic Tunnel Junctions Based on Hexagonal Boron Nitride. *ACS Nano* **2018**, *12* (5), 4712−4718.
(22) Zatko, V.; Galbiati, M.; Dubois, S. M.-M.; Och, M.; Palczynski, P.; Mattevi, C.; Brus, P.; Bezencenet, O.; Martin, M.-B.; Servet, B.; Charlier, J.-C.; Godel, F.; Vecchiola, A.; Bouzehouane, K.; Collin, S.; Petroff, F.; Dlubak, B.; Seneor, P. Band-Structure Spin-Filtering in Vertical Spin Valves Based on Chemical Vapor Deposited WS_2. *ACS Nano* **2019**, *13* (12), 14468−14476.
(23) Yang, H.; Vu, A. D.; Hallal, A.; Rougemaille, N.; Coraux, J.; Chen, G.; Schmid, A. K.; Chshiev, M. Anatomy and Giant Enhancement of the Perpendicular Magnetic Anisotropy of Cobalt-Graphene Heterostructures. *Nano Lett.* **2016**, *16* (1), 145−151.
(24) Lv, W.; Jia, Z.; Wang, B.; Lu, Y.; Luo, X.; Zhang, B.; Zeng, Z.; Liu, Z. Electric-Field Control of Spin-Orbit Torques in WS_2/Permalloy Bilayers. *ACS Appl. Mater. Interfaces* **2018**, *10* (3), 2843−2849.
(25) Yang, H.; Chen, G.; Cotta, A. A. C.; N'DIaye, A. T.; Nikolaev, S. A.; Soares, E. A.; MacEdo, W. A. A.; Liu, K.; Schmid, A. K.; Fert, A.; Chshiev, M. Significant Dzyaloshinskii−Moriya Interaction at Graphene-Ferromagnet Interfaces Due to the Rashba Effect. *Nat. Mater.* **2018**, *17* (7), 605−609.
(26) McDonnell, S. J.; Wallace, R. M. Atomically-Thin Layered Films for Device Applications Based upon 2D TMDC Materials. *Thin Solid Films* **2016**, *616*, 482−501.
(27) Briggs, N.; Subramanian, S.; Lin, Z.; Li, X.; Zhang, X.; Zhang, K.; Xiao, K.; Geohegan, D.; Wallace, R.; Chen, L.-Q.; Terrones, M.; Ebrahimi, A.; Das, S.; Redwing, J.; Hinkle, C.; Momeni, K.; van Duin, A.; Crespi, V.; Kar, S.; Robinson, J. A. A Roadmap for Electronic Grade 2D Materials. *2D Mater.* **2019**, *6* (2), 022001.
(28) Caneva, S.; Weatherup, R. S.; Bayer, B. C.; Blume, R.; Cabrero-Vilatela, A.; Braeuninger-Weimer, P.; Martin, M.-B.; Wang, R.; Baehtz, C.; Schloegl, R.; Meyer, J. C.; Hofmann, S. Controlling Catalyst Bulk Reservoir Effects for Monolayer Hexagonal Boron Nitride CVD. *Nano Lett.* **2016**, *16* (2), 1250−1261.
(29) Reina, A.; Jia, X.; Ho, J.; Nezich, D.; Son, H.; Bulovic, V.; Dresselhaus, M. S.; Kong, J. Large Area, Few-Layer Graphene Films on Arbitrary Substrates by Chemical Vapor Deposition. *Nano Lett.* **2009**, *9* (1), 30−35.
(30) Kidambi, P. R.; Ducati, C.; Dlubak, B.; Gardiner, D.; Weatherup, R. S.; Martin, M. B.; Seneor, P.; Coles, H.; Hofmann, S. The Parameter Space of Graphene Chemical Vapor Deposition on Polycrystalline Cu. *J. Phys. Chem. C* **2012**, *116* (42), 22492−22501.
(31) Reale, F.; Palczynski, P.; Amit, I.; Jones, G. F.; Mehew, J. D.; Bacon, A.; Ni, N.; Sherrell, P. C.; Agnoli, S.; Craciun, M. F.; Russo, S.; Mattevi, C. High-Mobility and High-Optical Quality Atomically Thin WS_2. *Sci. Rep.* **2017**, *7* (1), 14911.
(32) Zhou, J.; Lin, J.; Huang, X.; Zhou, Y.; Chen, Y.; Xia, J.; Wang, H.; Xie, Y.; Yu, H.; Lei, J.; Wu, D.; Liu, F.; Fu, Q.; Zeng, Q.; Hsu, C. H.; Yang, C.; Lu, L.; Yu, T.; Shen, Z.; Lin, H.; Yakobson, B. I.; Liu, Q.; Suenaga, K.; Liu, G.; Liu, Z. A Library of Atomically Thin Metal Chalcogenides. *Nature* **2018**, *556* (7701), 355−359.
(33) Yan, M.; Wang, E.; Zhou, X.; Zhang, G.; Zhang, H.; Zhang, K.; Yao, W.; Lu, N.; Yang, S.; Wu, S.; Yoshikawa, T.; Miyamoto, K.; Okuda, T.; Wu, Y.; Yu, P.; Duan, W.; Zhou, S. High Quality Atomically Thin $PtSe_2$ Films Grown by Molecular Beam Epitaxy. *2D Mater.* **2017**, *4* (4), 045015.
(34) Nakano, M.; Wang, Y.; Kashiwabara, Y.; Matsuoka, H.; Iwasa, Y. Layer-by-Layer Epitaxial Growth of Scalable WSe_2 on Sapphire by Molecular Beam Epitaxy. *Nano Lett.* **2017**, *17* (9), 5595−5599.
(35) Vergnaud, C.; Gay, M.; Alvarez, C.; Dau, M.-T.; Pierre, F.; Jalabert, D.; Licitra, C.; Marty, A.; Beigné, C.; Grévin, B.; Renault, O.; Okuno, H.; Jamet, M. Van Der Waals Solid Phase Epitaxy to Grow Large-Area Manganese-Doped $MoSe_2$ Few-Layers on SiO_2/Si. *2D Mater.* **2019**, *6* (3), 035019.
(36) Loh, T. A. J.; Chua, D. H. C.; Wee, A. T. S. One-Step Synthesis of Few-Layer WS_2 by Pulsed Laser Deposition. *Sci. Rep.* **2016**, *5* (1), 18116.
(37) Yao, J. D.; Zheng, Z. Q.; Shao, J. M.; Yang, G. W. Stable, Highly-Responsive and Broadband Photodetection Based on Large-Area Multilayered WS_2 Films Grown by Pulsed-Laser Deposition. *Nanoscale* **2015**, *7* (36), 14974−14981.
(38) Serna, M. I.; Yoo, S. H.; Moreno, S.; Xi, Y.; Oviedo, J. P.; Choi, H.; Alshareef, H. N.; Kim, M. J.; Minary-Jolandan, M.; Quevedo-Lopez, M. A. Large-Area Deposition of MoS_2 by Pulsed Laser Deposition with in Situ Thickness Control. *ACS Nano* **2016**, *10* (6), 6054−6061.

https://dx.doi.org/10.1021/acsanm.0c01408
ACS Appl. Nano Mater. 2020, 3, 7908−7916

(39) Contour, J.-P.; Couvert, C.; Durand, O.; Lemaître, Y.; Lyonnet, R.; Marcilhac, B. Suppression of the "notch Effect" in Microwave Surface Resistance in $YBa_2Cu_3O_7$ Films on MgO (100) Substrate by Deposition of Ultra-Thin $SrTiO_3$ Seed Layers. *Eur. Phys. J.: Appl. Phys.* **1999**, *5* (1), 3−8.
(40) Bouzehouane, K.; Woodall, P.; Marcilhac, B.; Khodan, A. N.; Crété, D.; Jacquet, E.; Mage, J. C.; Contour, J. P. Enhanced Dielectric Properties of $SrTiO_3$ Epitaxial Thin Film for Tunable Microwave Devices. *Appl. Phys. Lett.* **2002**, *80* (1), 109−111.
(41) De Teresa, J. M.; Barthélémy, A.; Fert, A.; Contour, J. P.; Montaigne, F.; Seneor, P. Role of Metal-Oxide Interface in Determining the Spin Polarization of Magnetic Tunnel Junctions. *Science* **1999**, *286* (5439), 507−509.
(42) Gajek, M.; Bibes, M.; Fusil, S.; Bouzehouane, K.; Fontcuberta, J.; Barthélémy, A.; Fert, A. Tunnel Junctions with Multiferroic Barriers. *Nat. Mater.* **2007**, *6* (4), 296−302.
(43) Soumah, L.; Beaulieu, N.; Qassym, L.; Carrétéro, C.; Jacquet, E.; Lebourgeois, R.; Ben Youssef, J.; Bortolotti, P.; Cros, V.; Anane, A. Ultra-Low Damping Insulating Magnetic Thin Films Get Perpendicular. *Nat. Commun.* **2018**, *9* (1), 3355.
(44) Govind Rajan, A.; Warner, J. H.; Blankschtein, D.; Strano, M. S. Generalized Mechanistic Model for the Chemical Vapor Deposition of 2D Transition Metal Dichalcogenide Monolayers. *ACS Nano* **2016**, *10* (4), 4330−4344.
(45) Lee, J.; Pak, S.; Giraud, P.; Lee, Y.-W.; Cho, Y.; Hong, J.; Jang, A.-R.; Chung, H.-S.; Hong, W.-K.; Jeong, H. Y.; Shin, H. S.; Occhipinti, L. G.; Morris, S. M.; Cha, S.; Sohn, J. I.; Kim, J. M. Thermodynamically Stable Synthesis of Large-Scale and Highly Crystalline Transition Metal Dichalcogenide Monolayers and Their Unipolar n-n Heterojunction Devices. *Adv. Mater.* **2017**, *29* (33), 1702206.
(46) Berkdemir, A.; Gutiérrez, H. R.; Botello-Méndez, A. R.; Perea-López, N.; Elías, A. L.; Chia, C. I.; Wang, B.; Crespi, V. H.; López-Urías, F.; Charlier, J. C.; Terrones, H.; Terrones, M. Identification of Individual and Few Layers of WS_2 Using Raman Spectroscopy. *Sci. Rep.* **2013**, *3* (1), 1755.
(47) Loh, T. A. J.; Chua, D. H. C. Origin of Hybrid 1T- and 2H-WS_2 Ultrathin Layers by Pulsed Laser Deposition. *J. Phys. Chem. C* **2015**, *119* (49), 27496−27504.
(48) Terrones, H.; Del Corro, E.; Feng, S.; Poumirol, J. M.; Rhodes, D.; Smirnov, D.; Pradhan, N. R.; Lin, Z.; Nguyen, M. A. T.; Elías, A. L.; Mallouk, T. E.; Balicas, L.; Pimenta, M. A.; Terrones, M. New First Order Raman-Active Modes in Few Layered Transition Metal Dichalcogenides. *Sci. Rep.* **2015**, *4*, 4215.
(49) Iqbal, M. Z.; Iqbal, M. W.; Siddique, S.; Khan, M. F.; Ramay, S. M. Room Temperature Spin Valve Effect in NiFe/WS_2/Co Junctions. *Sci. Rep.* **2016**, *6*, 21038.
(50) Dankert, A.; Pashaei, P.; Kamalakar, M. V.; Gaur, A. P. S.; Sahoo, S.; Rungger, I.; Narayan, A.; Dolui, K.; Hoque, M. A.; Patel, R. S.; de Jong, M. P.; Katiyar, R. S.; Sanvito, S.; Dash, S. P. Spin-Polarized Tunneling through Chemical Vapor Deposited Multilayer Molybdenum Disulfide. *ACS Nano* **2017**, *11* (6), 6389−6395.
(51) Galbiati, M.; Tatay, S.; Dubois, S. M. M.; Godel, F.; Galceran, R.; Mañas-Valero, S.; Piquemal-Banci, M.; Vecchiola, A.; Charlier, J. C.; Forment-Aliaga, A.; Coronado, E.; Dlubak, B.; Seneor, P. Path to Overcome Material and Fundamental Obstacles in Spin Valves Based on MoS_2 and Other Transition-Metal Dichalcogenides. *Phys. Rev. Appl.* **2019**, *12* (4), 044022.
(52) Weatherup, R. S.; Amara, H.; Blume, R.; Dlubak, B.; Bayer, B. C.; Diarra, M.; Bahri, M.; Cabrero-Vilatela, A.; Caneva, S.; Kidambi, P. R.; Martin, M.-B.; Deranlot, C.; Seneor, P.; Schloegl, R.; Ducastelle, F.; Bichara, C.; Hofmann, S. Interdependency of Subsurface Carbon Distribution and Graphene-Catalyst Interaction. *J. Am. Chem. Soc.* **2014**, *136* (39), 13698−13708.
(53) Biesinger, M. C.; Payne, B. P.; Lau, L. W. M.; Gerson, A.; Smart, R. S. C. X-Ray Photoelectron Spectroscopic Chemical State Quantification of Mixed Nickel Metal, Oxide and Hydroxide Systems. *Surf. Interface Anal.* **2009**, *41* (4), 324−332.
(54) Dlubak, B.; Martin, M. B.; Weatherup, R. S.; Yang, H.; Deranlot, C.; Blume, R.; Schloegl, R.; Fert, A.; Anane, A.; Hofmann, S.; Seneor, P.; Robertson, J. Graphene-Passivated Nickel as an Oxidation-Resistant Electrode for Spintronics. *ACS Nano* **2012**, *6* (12), 10930−10934.
(55) Galbiati, M.; Tatay, S.; Barraud, C.; Dediu, A. V.; Petroff, F.; Mattana, R.; Seneor, P. Spinterface: Crafting Spintronics at the Molecular Scale. *MRS Bull.* **2014**, *39* (07), 602−607.
(56) Kim, T.; Moodera, J. Large Spin Polarization in Epitaxial and Polycrystalline Ni Films. *Phys. Rev. B: Condens. Matter Mater. Phys.* **2004**, *69* (2), 020403.
(57) Popinciuc, M.; Józsa, C.; Zomer, P. J.; Tombros, N.; Veligura, A.; Jonkman, H. T.; van Wees, B. J. Electronic Spin Transport in Graphene Field-Effect Transistors. *Phys. Rev. B: Condens. Matter Mater. Phys.* **2009**, *80* (21), 214427.
(58) Dlubak, B.; Martin, M.-B.; Deranlot, C.; Servet, B.; Xavier, S.; Mattana, R.; Sprinkle, M.; Berger, C.; De Heer, W. A.; Petroff, F.; Anane, A.; Seneor, P.; Fert, A. Highly Efficient Spin Transport in Epitaxial Graphene on SiC. *Nat. Phys.* **2012**, *8* (7), 557−561.
(59) Safeer, C. K.; Ingla-Aynés, J.; Herling, F.; Garcia, J. H.; Vila, M.; Ontoso, N.; Calvo, M. R.; Roche, S.; Hueso, L. E.; Casanova, F. Room-Temperature Spin Hall Effect in Graphene/MoS_2 van Der Waals Heterostructures. *Nano Lett.* **2019**, *19*, 1074.
(60) Island, J. O.; Cui, X.; Lewandowski, C.; Khoo, J. Y.; Spanton, E. M.; Zhou, H.; Rhodes, D.; Hone, J. C.; Taniguchi, T.; Watanabe, K.; Levitov, L. S.; Zaletel, M. P.; Young, A. F. Spin-Orbit-Driven Band Inversion in Bilayer Graphene by the van Der Waals Proximity Effect. *Nature* **2019**, *571* (7763), 85−89.
(61) Yang, H.; Chen, G.; Cotta, A. A. C.; N'DIaye, A. T.; Nikolaev, S. A.; Soares, E. A.; MacEdo, W. A. A.; Liu, K.; Schmid, A. K.; Fert, A.; Chshiev, M. Significant Dzyaloshinskii-Moriya Interaction at Graphene-Ferromagnet Interfaces Due to the Rashba Effect. *Nat. Mater.* **2018**, *17* (7), 605−609.
(62) Liang, J.; Wang, W.; Du, H.; Hallal, A.; Garcia, K.; Chshiev, M.; Fert, A.; Yang, H. Very Large Dzyaloshinskii-Moriya Interaction in Two-Dimensional Janus Manganese Dichalcogenides and Its Application to Realize Skyrmion States. *Phys. Rev. B: Condens. Matter Mater. Phys.* **2020**, *101* (18), 184401.
(63) Shao, Q.; Yu, G.; Lan, Y. W.; Shi, Y.; Li, M. Y.; Zheng, C.; Zhu, X.; Li, L. J.; Amiri, P. K.; Wang, K. L. Strong Rashba-Edelstein Effect-Induced Spin-Orbit Torques in Monolayer Transition Metal Dichalcogenide/Ferromagnet Bilayers. *Nano Lett.* **2016**, *16* (12), 7514−7520.
(64) Ahn, E. C. 2D Materials for Spintronic Devices. *npj 2D Mater. Appl.* **2020**, *4*, 17.
(65) Liu, Y.; Shao, Q. Two-Dimensional Materials for Energy-Efficient Spin-Orbit Torque Devices. *ACS Nano* **2020**, *2003*, 11966.
(66) Loh, T. A. J.; Chua, D. H. C. Growth Mechanism of Pulsed Laser Fabricated Few-Layer MoS_2 on Metal Substrates. *ACS Appl. Mater. Interfaces* **2014**, *6* (18), 15966−15971.
(67) Serrao, C. R.; Diamond, A. M.; Hsu, S. L.; You, L.; Gadgil, S.; Clarkson, J.; Carraro, C.; Maboudian, R.; Hu, C.; Salahuddin, S. Highly Crystalline MoS_2 Thin Films Grown by Pulsed Laser Deposition. *Appl. Phys. Lett.* **2015**, *106* (5), 052101.
(68) Siegel, G.; Venkata Subbaiah, Y. P.; Prestgard, M. C.; Tiwari, A. Growth of Centimeter-Scale Atomically Thin MoS_2 Films by Pulsed Laser Deposition. *APL Mater.* **2015**, *3* (5), 056103.
(69) Yang, Z.; Hao, J. Progress in Pulsed Laser Deposited Two-Dimensional Layered Materials for Device Applications. *J. Mater. Chem. C* **2016**, *4* (38), 8859−8878.
(70) Barvat, A.; Prakash, N.; Satpati, B.; Singha, S. S.; Kumar, G.; Singh, D. K.; Dogra, A.; Khanna, S. P.; Singha, A.; Pal, P. Emerging Photoluminescence from Bilayer Large-Area 2D MoS_2 Films Grown by Pulsed Laser Deposition on Different Substrates. *J. Appl. Phys.* **2017**, *122* (1), 015304.
(71) Yang, Z.; Wu, Z.; Lyu, Y.; Hao, J. Centimeter-scale Growth of Two-dimensional Layered High-mobility Bismuth Films by Pulsed Laser Deposition. *InfoMat* **2019**, *1* (1), 98−107.

https://dx.doi.org/10.1021/acsanm.0c01408
ACS Appl. Nano Mater. 2020, 3, 7908−7916

(72) Bai, G.; Lyu, Y.; Wu, Z.; Xu, S.; Hao, J. Lanthanide Near-Infrared Emission and Energy Transfer in Layered WS_2/MoS_2 Heterostructure. *Sci. China Mater.* **2020**, *63* (4), 575−581.
(73) Tian, K.; Baskaran, K.; Tiwari, A. Growth of Two-Dimensional WS_2 Thin Films by Pulsed Laser Deposition Technique. *Thin Solid Films* **2018**, *668*, 69−73.
(74) Dieny, B.; Prejbeanu, I. L.; Garello, K.; Gambardella, P.; Freitas, P.; Lehndorff, R.; Raberg, W.; Ebels, U.; Demokritov, S. O.; Akerman, J.; Deac, A.; Pirro, P.; Adelmann, C.; Anane, A.; Chumak, A. V.; Hiroata, A.; Mangin, S.; Onbasli, M. C.; Aquino, M. d; Prenat, G.; Finocchio, G.; Diaz, L. L.; Chantrell, R.; Fesenko, O. C.; Bortolotti, P. Opportunities and Challenges for Spintronics in the Microelectronic Industry. *Arxiv.com* **2019**, *1908*, 10584.
(75) Kosmider, K.; González, J. W.; Fernández-Rossier, J. Large Spin Splitting in the Conduction Band of Transition Metal Dichalcogenide Monolayers. *Phys. Rev. B: Condens. Matter Mater. Phys.* **2013**, *88* (24), 245436.
(76) Wang, G.; Robert, C.; Suslu, A.; Chen, B.; Yang, S.; Alamdari, S.; Gerber, I. C.; Amand, T.; Marie, X.; Tongay, S.; Urbaszek, B. Spin-Orbit Engineering in Transition Metal Dichalcogenide Alloy Monolayers. *Nat. Commun.* **2015**, *6* (1), 10110.

https://dx.doi.org/10.1021/acsanm.0c01408
ACS Appl. Nano Mater. 2020, 3, 7908−7916